A CONTINUOUS-FLOW GAS INTERFACE OF A THERMAL/OPTICAL ANALYZER WITH ^{14}C AMS FOR SOURCE APPORTIONMENT OF ATMOSPHERIC AEROSOLS

Konstantinos Agrios[1,2,3] • Gary Salazar[1,2]* • Sönke Szidat[1,2]

[1]Department of Chemistry and Biochemistry, University of Bern, Bern, Switzerland.
[2]Oeschger Centre for Climate Change Research, University of Bern, Bern, Switzerland.
[3]Laboratory of Radiochemistry, Paul Scherrer Institute (PSI), Villigen, Switzerland.

ABSTRACT. This article reports on the performance of a continuous-flow interface for CO_2 gas feeding into the ion source of a 200-kV accelerator mass spectrometer (AMS) in splitless mode. Distinct CO_2 fractions and subfractions produced by a commercial Sunset OC/EC (organic carbon/elemental carbon) analyzer from ambient atmospheric aerosols filters are injected into the source and then analyzed by their $^{14}C/^{12}C$ ratio in real time. New features are revealed from organic aerosol subfractions, which thermally desorb close to each other and are only visible by real-time analysis. An optimized setup for this purpose is presented for the measurement of CO_2 amounts from 3 to 45 µg C. Efficiencies of 4.5–8.0% for the formation of C^- ions from CO_2 are obtained for sample masses of 5–10 µg C and carbon mass flow rates below 2 µg min^{-1}. However, this ionization efficiency is substantially suppressed at high carbon mass flow rates. The potential of this method for a refined apportionment of aerosol sources is demonstrated with ambient filter samples.

KEYWORDS: AMS, atmospheric carbonaceous aerosols, carbon dioxide, gas analysis,[14]C.

INTRODUCTION

Organic aerosols (OAs) comprise a significant portion of the atmospheric fine particulate matter and their concentration mainly depends on the geographic position. It has been shown that OA concentrations can amount to 20–50% at continental midlatitudes and up to 90% in tropical forests (Kanakidou et al. 2005). Depending on its chemical composition, OA may have a negative influence on both human health and climate. OAs are classified into primary OA (POA) and secondary OA (SOA). POAs are composed of organic compounds that are directly emitted into the atmosphere as particulate matter from different sources. The primary fraction can also contain a considerable amount of inorganic substances. The SOA fraction is produced in the atmosphere by oxidation of volatile organic compounds (VOCs), reducing their volatility so that they partition from the gas to the aerosol phase (Robinson et al. 2007; De Gouw and Jimenez 2009; Hodzic et al. 2010). The total carbon (TC) from the OA is divided into two fractions, i.e. organic carbon (OC) and elemental carbon (EC), of which OC comprises less refractory, non-light-absorbing chemical species and EC consists of highly polymerized and optically active structures (Pöschl 2005). These two fractions can be separated using thermo-optical devices like the commercial Sunset OC/EC analyzer using specified protocols like Swiss_4S (Zhang et al. 2012).

Radiocarbon measurements with accelerator mass spectrometry (AMS) can apportion organic aerosol emissions into fossil and nonfossil sources and quantify such emissions (Szidat 2009). This speciation relies on the principle that ^{14}C is extinct in fossil material ($F^{14}C = 0$), whereas in modern materials ^{14}C is found on the contemporary level ($F^{14}C \sim 1$). The ^{14}C analysis should be performed separately in OC and EC, since both fractions have different emission origins and affect human health and Earth climate differently (Szidat et al. 2004a, 2004b, 2006; Pöschl 2005; Currie and Kessler 2005; Szidat 2009).

Currently, we perform ^{14}C analysis of ambient aerosol samples by using various analytical combustion instruments coupled to a MICADAS (Mini Carbon DAting System) AMS by means of a gas inlet system (GIS). The analysis involves OC/EC thermal separation,

---

*Corresponding author. Email: gary.salazar@dcb.unibe.ch.

combustion, trapping the CO_2 pulse, releasing the gas, and slow injection or infusion into the ion source where the CO_2 is converted into C^-, O^-, as well as other ionic and neutral species (Perron et al. 2010; Ruff et al. 2010; Wacker et al. 2013; Agrios et al. 2015; Salazar et al. 2015). This coupling allows for high-throughput routine ^{14}C analysis of aerosols with small carbon mass (>10 µg C). It is possible to analyze the OC and EC fractions separately from one sample with the Sunset OC/EC analyzer coupled to the GIS-AMS system in an online trapping mode (Agrios et al. 2015) because the separation protocol allows for a time gap between the OC and EC peaks of around 20 min. However, subfractions separated with a modified thermal ramp cannot be analyzed by trapping the CO_2 because these subfractions appear too close to each other. Therefore, for improved source apportionment an interface is required that injects the CO_2 from the separated subfractions in a real-time continuous-flow mode into the AMS. This paper continues the study of a continuous-flow interface developed earlier (Agrios et al. 2015). Here, we characterize and validate the interface using standard materials. In addition, this paper shows the application of this interface to the ^{14}C analysis of thermal subfractions of OC for selected atmospheric aerosol filters as examples of its performance.

MATERIALS AND METHODS

Sunset OC/EC Analyzer and Temperature Programs

Samples and standard materials are loaded on prebaked quartz filters in a Sunset OC/EC analyzer (Model4L, Sunset Laboratory, USA), which is specially equipped with a nondispersive infrared (NDIR) detector (Zhang et al. 2012). The Sunset OC/EC analyzer thermally desorbs and/or combusts aerosol samples by applying a temperature ramp. Afterwards, the evolving products are oxidized catalytically, producing a pulse of CO_2 gas, which then passes through the NDIR and a H_2O trap containing Sicapent (Merck, Germany) entering the interface, which is connected to the AMS instrument. Here, the CO_2 is ionized and detected as a [12]C^- peak in a Faraday cup on the low-energy side of the AMS. The setup of the system and a proof-of-principle of this method was described by Agrios et al. (2015).

Three different thermal protocols, termed the TC, OC/EC, and OC subfraction, are used in this work. Pure O_2 (99.9995%) is used as carrier gas in order to diminish the charring effect that takes place in anoxic conditions (Zhang et al. 2012). In the total carbon (TC) protocol, only one step is used at 760°C for 400 s. Our OC/EC thermal protocol is based on the 4-step Swiss_4S protocol (for details see Zhang et al. 2012), but excluding the intermediate helium step. Our OC/EC protocol defines OC as the aerosol fraction that combusts in pure oxygen at 375°C for 400 s in the first step. Then, residual OC is completely removed in pure oxygen at 475°C for 400 s in the second step, where some premature EC evolution occurs as well, and subsequently EC is combusted in pure oxygen at 680°C for 300 s in third step. Two protocols are used to separate the OC subfractions. Their temperature steps are 200, 260, 300, and 375°C for the first protocol and 200 and 375°C for the second protocol with a total duration of 400 s for both protocols. Cooling is not applied between the different steps in order to ensure complete desorption of less volatile components and diminish peak-to-peak carryover. The duration of the thermal steps is long enough to allow baseline separation of the [12]C^- peaks.

Reference Materials

C7 (oxalic acid), C6 (sucrose), and C5 (wood) are reference materials from the International Atomic Energy Agency (IAEA) (Rozanski et al. 1992; Le Clercq et al. 1998). The primary standard oxalic acid II (HOxII, SRM 4990C) is provided by the National Institute of Standards and Technology (NIST) and ^{14}C-free material sodium acetate (NaOAc, p.a.) from Merck.

Table 1 $^{14}C/^{12}C$ analysis of IAEA standards (Rozanski et al. 1992; Le Clercq et al. 1998) using the continuous-flow method with 1σ uncertainties for $n = 3$ repetitions for each material. Measured carbon amounts ranged between 15 and 20 µg C. The P value describes the level of significance from a t test comparing nominal and measured $F^{14}C$, indicating a statistically significant difference for P values < 0.05.

Reference material	Nominal $F^{14}C$	Measured $F^{14}C$	P value
C5	0.231 ± 0.0002	0.237 ± 0.008	0.32
C7	0.495 ± 0.001	0.497 ± 0.014	0.83
C6	1.506 ± 0.001	1.512 ± 0.039	0.81

They are used for standard normalization and blank subtraction, respectively. Measured $F^{14}C$ values of the standards are given in Table 1. The standards are analyzed with the TC protocol. Grains of the standard materials are loaded on a clean filter and combusted on the sample holder of Sunset OC/EC analyzer. For the calibration of the Sunset OC/EC analyzer, aqueous solutions of sucrose (Sigma Aldrich, D(+)-Sucrose, Fluka Analytical) are employed. Some 5–10 µL from sucrose stock solutions of 1–10 µg/µL are pipetted on 1.5-cm^2 prebaked quartz-fiber filters. The wet samples are inserted in the Sunset OC/EC analyzer sample holder and dried during 2 min at 70°C under a helium stream before initiating the total carbon combustion temperature program.

Ambient Aerosol Filters

Ambient aerosol filters were selected from different sites: (a) from an urban background station in Zurich, Switzerland, which is located in a park-like courtyard in the city center close to the main railway station (Szidat et al. 2004a; Zotter et al. 2014a); (b) from a suburban station in Sissach, Switzerland, which is influenced by local traffic (Zotter et al. 2014a); as well as (c) from a suburban station on the Caltech campus in Pasadena, CA, as part of the CalNex 2010 field campaign in the Los Angeles Basin, which aimed at studying the urban plume from Los Angeles and the regional background air (Zotter et al. 2014b). The samples from Zurich and Sissach were heavily loaded with particulate matter containing typically 30 and 10 µg C/cm^2 for OC and EC, respectively. Filters from Los Angeles were loaded with low amounts of 10 µg C/cm^2 TC. For the combustion of the Zurich filters, a 0.3-cm^2 quartz filter punch per sample is used. In the case of the Los Angeles filters, three 1.5-cm^2 quartz filter punches (i.e. the normal size of the Sunset EC/OC analyzer) were piled up in the sample holder due to the low loading of the samples. Therefore, it should be noted that O_2 carrier may have accessed the surface of each piled filter inhomogeneously during combustion. We cannot exclude that this situation may have produced artifacts during the measurement.

Cu Reduction Reactor Interface

The direct coupling of the Sunset OC/EC analyzer to the MICADAS requires that the O_2 carrier gas excess is scrubbed away prior to the CO_2 pulse feeding into the ion source. For this reason, we employ a heated reactor filled with Cu wire bits that has been described before by Agrios et al. (2015). In brief, the oxygen combusts the samples and the CO_2 gas is carried through an oven filled with MnO_2, an NDIR detector, and then through a H_2O trap. Afterwards, the exhaust stream passes through the heated Cu reactor, forming copper oxide and reducing the O_2 flow from 20 mL/min down to ~0 mL/min. Since the O_2 is scrubbed away, an additional, minimal He carrier flow is added after the exhaust of the H_2O trap via a union Tee

and in front of the Cu reactor. This allows the CO_2 to be transported into the ion source in a splitless mode via a 90-cm-long fused silica capillary located after the Cu reactor. The minimal He flow is continuously supplied at flow rates that maintain the high vacuum and ionization efficiency of the ion source. The normal pressure range in the ion source of our MICADAS AMS is 4 to 10×10^{-6} hPa, which limits feasible inner diameters (ID) of the inlet capillary to 0.10–0.13 mm. We use He carrier flow rates of 1–4 mL/min as a compromise, which are high enough to overcome dead volumes and sample losses, but low enough to keep the vacuum of the ion source.

^{14}C Analysis

The 200kV AMS MICADAS installed at the Laboratory for the Analysis of Radiocarbon with AMS (LARA) uses a gas ion source, which accepts CO_2 (Wacker et al. 2013; Szidat et al. 2014). The measured ^{14}C/^{12}C ratios are presented as absolute ratios as qualitative information or as F^{14}C values as defined by Reimer et al. (2004). During gas feeding, the ^{14}C counting and the stable isotopes currents are averaged every 3 s. To calculate the sample F^{14}C, the ^{14}C from the blank and the residual isobaric molecular interference are subtracted from the ^{14}C/^{12}C ratio. Then, the ratio is corrected for fractionation with the ^{13}C/^{12}C ratio and normalized with the ^{14}C/^{12}C ratio of the standard.

RESULTS AND DISCUSSION

The results for the continuous-flow Sunset OC/EC analyzer coupling to the MICADAS AMS consist of three main parts: method optimization, validation, and application to real samples. In the method optimization, we first study how to control the carbon mass flow within the injected pulse of CO_2 delivered into the ion source. Secondly, we show how the carbon mass flow affects the ionization efficiency. For the real samples, we investigate the thermal separation of the OC subfractions by measuring the ^{14}C/^{12}C ratio in real time.

Method Optimization: Controlling Carbon Mass Flow Rate

Figure 1 illustrates the behavior of the ^{12}C$^-$ current when continuous-flow CO_2 pulses are injected into the ion source. Due to the dead volume of the Cu reactor, the ^{12}C$^-$ peaks are broader by a factor of 1.5 in comparison to the NDIR peaks. Figures 1a and 1b show a minimum of the ^{12}C$^-$ current in the middle of the peak for C mass flows of 1.54 and 2.4 µg C/min, respectively. [The carbon mass flow is defined as the carbon mass injected divided by the time of the full width at half maximum (FWHM) of the ^{12}C$^-$ peak.] The drop of the ^{12}C$^-$ current happens at relatively low He carrier flow rate (2.5 mL/min) or high carbon masses (20 µg C). This inconvenient ionization suppression causes double peaks from single CO_2 injections. It is known that the O$^-$ signal is much higher than the C$^-$ signal for direct gas ionization as shown by Fahrni et al. (2013). At high carbon mass flows, the CO_2 concentration at the target is higher; therefore, it is possible that the oxygen capture most of the available electrons, suppressing the C$^-$ formation (Salazar et al. 2016). The feeding of the CO_2 pulse into the ion source with a continuous-flow system cannot be kept as constant and controllable as performed by the gas-tight syringe of the GIS. Controlling the C mass flow depends on knowing the CO_2 partial pressure and the pressure at both sides of the ion source inlet capillary, which are unknown for a CO_2 pulse injection system.

Because the C mass flow affects the signal, it is important to find out how to control it by changing the He carrier flow, the dimensions of the inlet capillary, and combusting different carbon masses. In Figure 2a, the helium carrier gas flow rate is kept constant but the carbon mass is changed in the range of 3–50 µg C, causing the carbon mass flow to increase linearly.
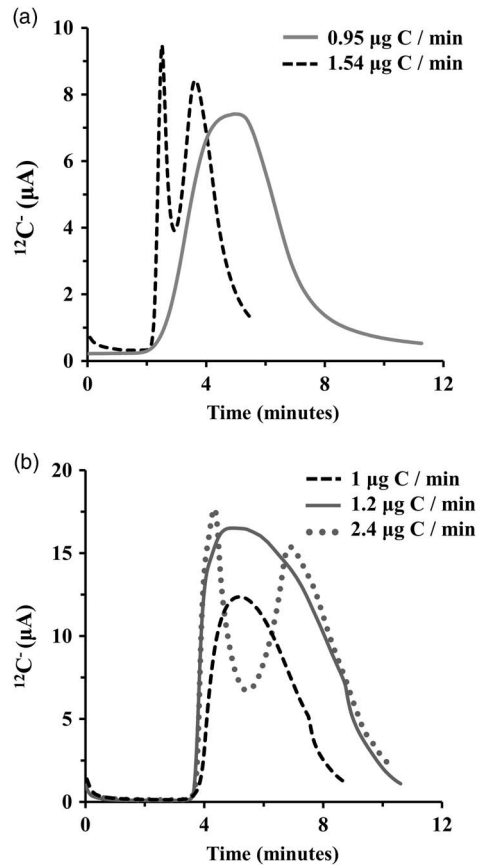
(a)

(b)

Figure 1 $^{12}C^-$ currents from the analysis of HOxII: (a) 6 μg C transported to the ion source by using a 0.13-mm-ID inlet capillary at 2.5 mL min^{-1} (dashed line) and 3.5 mL min^{-1} (solid line) He carrier flow rate; and (b) 6 μg C (dashed black line), 10 μg C (red solid line), and 20 μg C delivered (dotted line) via a 0.10-mm-ID inlet capillary and at a constant He carrier flow rate of 1.5 mL min^{-1}. Corresponding average carbon mass flow rates are indicated in the legend.

Injections of samples higher than 10 μg C are affected by the ionization suppression and such measurements are denoted with a cross symbol in the graph. In Figure 2b, the sample mass is constant at 6 μg C (HOxII) and injections with different He carrier flow rates are performed. The carbon mass flow exhibits a linear relationship with the inverse of the He carrier flow. This reveals that the C mass flow is directly proportional to the injected mass and inversely proportional to the He carrier flow. The importance of these relationships among the experimental parameters allow us to control the carbon mass flow of the analysis.

Method Optimization: Effect of Carbon Mass Flow Rate on the Ionization

Figure 3a demonstrates how the negative ionization is affected by the carbon mass flow rate. For a constant mass of 6 μg C HOxII, we trace the behavior of the system for He carrier flows
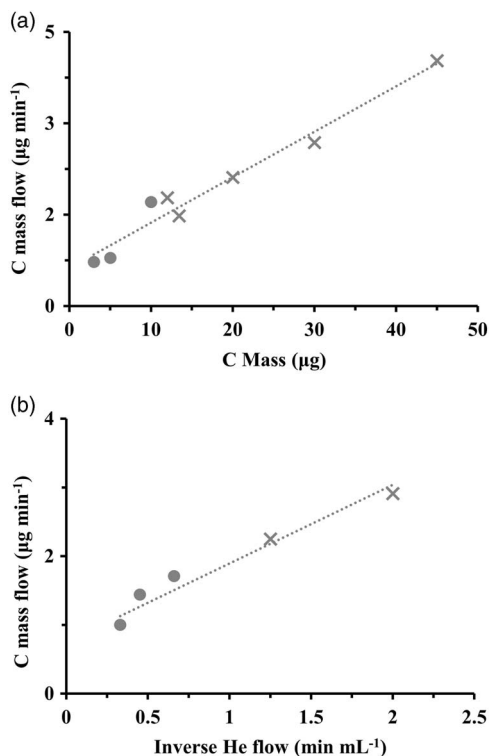
Figure 2 Carbon mass flow rate of HOxII depending on (a) the C mass injected at 1.5 mL min^{-1} and (b) the inverse of the He flow using 6 µg C and He flows of 0.5–3.5 mL/min. Measurements with ionization suppression are indicated by crosses. In all measurements, CO_2 was transported to the ion source using a 0.10-mm-ID inlet capillary. Same experimental details as in Figure 1.

between 0.5 and 3.5 mL min^{-1}. For higher carrier flow rates, eventually the $^{12}C^{-}$ signal is lost due to back-pressure exerted by the narrow capillary. The ionization suppression starts at a certain carbon mass flow rate as indicated by the transition between the closed symbols and the asterisks. For our instrumental setup, the suppression thresholds are ~1.8 and ~1.25 µg/min depending on the capillary ID. As indicated before, the suppression may be due to the high concentration of oxygen from CO_2 suppressing the C^- formation. For the 0.13-mm ID, it seems to be possible to achieve higher efficiencies, but those measurements are affected by ionization suppression. The 0.10-mm-ID capillary enables a wider range of flows with unsuppressed signal. Unfortunately, in our case it is not possible to use higher He carrier flow rates than 1.5 mL min^{-1} for the smaller capillary because the back-pressure affects the performance of the Sunset OC/EC analyzer. It should be noted, however, that the strong differences between the ionization yields for both capillaries may partially be caused from day-to-day changes of the state of the ion source.

In the ion source of MICADAS, the CO_2 is sputtered by Cs^+ after it has diffused on the cathode front via a narrow borehole (Fahrni et al. 2013). Therefore, we used gas targets with a
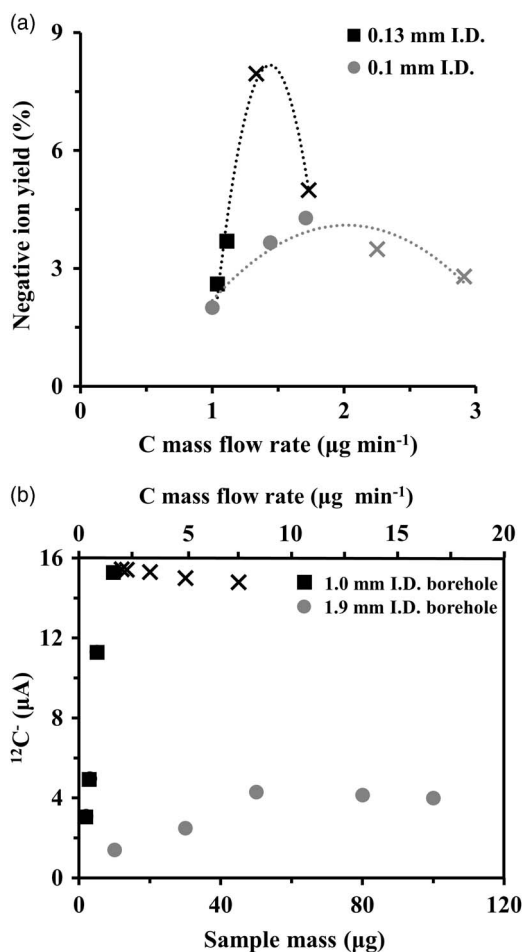
Figure 3 Influence of the carbon mass flow rate on (a) ionization yields using fixed sample masses of 6 μg C and variable He flows and (b) $^{12}C^-$ currents depending on the mass of the sample and geometry of the gas target. Measurements with ionization suppression are indicated by crosses. Same experimental details as in Figure 1.

1.9-mm-ID borehole size in order to study how this affects the C^- formation in comparison with the original gas targets with 1.0-mm-ID borehole size (Figure 3b). Since the He flow rate is kept constant, the C mass flow rate is the same for the two targets of different borehole size, when same carbon masses are injected. However, the $^{12}C^-$ currents and ionization efficiency are higher for the 1.0-mm-ID. borehole at every point in Figure 3b. For the 1.9-mm-ID borehole, ionization suppression is not visible within the presented CO_2 mass range. We believe that these features are due to the lower partial pressure of CO_2 when diffusing through the larger volume of the 1.9-mm-ID borehole. Therefore, the ionization not only depends on the carbon mass flow rate, but also in the CO_2 concentration at the target surface. Both parameters, the ID of the capillary and the borehole size of the target, should be investigated further in order to optimize measurement conditions for smaller versus larger samples.

Validation

Table 1 presents mean values from three injections per standard material (C5, C6, and C7) taken with the TC protocol using a He flow of 1.5 mL min^{-1} and inlet capillary of 0.10 mm ID. The individual F^{14}C values are calculated by averaging the isotope ratios over the FWHM of the ^{12}C$^-$ peak. Only one grain of standard material was used per measurement and its carbon mass ranges from 15 to 20 µg. In general, ^{13}C/^{12}C and ^{14}C/^{12}C ratios are relatively stable during the ionization suppression that occurs while injecting standard material from 15 to 45 µg C. The resulting peak broadening caused by the high C mass flow rates extends the measurement time and this leads to higher number of ^{14}C counts and, therefore, to a lower uncertainty. Analyses of HOxII samples between 3 and 45 µg C provided 1274 to 12,031 ^{14}C counts, obtaining measurement uncertainties from 5% to 1.5%, respectively. All the P values calculated from the t test comparison between the F^{14}C of the respective reference value and our measurement are much larger than the significance level of 0.05. This indicates that there is no statistically significant difference between both values for all standards.

By following the same procedure as Salazar et al. (2015) for measuring constant and cross-contamination, solid samples spanning different sizes of fossil NaOAc and modern HOxII were combusted in order to estimate the constant and cross-contamination of the Sunset OC/EC analyzer system coupled to the Cu reactor. The system induces a constant contamination mass of 0.6 ± 0.1 µg C with an F^{14}C value of 0.75 ± 0.05, which is comparable to conditions when the Sunset OC/EC analyzer is connected to the GIS using the trap (Agrios et al. 2015). The cross-contamination factor of the system was estimated by combusting the fossil and modern materials alternately and in separate runs with fresh targets. We estimate that $1.4 \pm 0.6\%$ of the previous sample remains and cross-contaminates the following measurement. This is substantially higher than for the GIS trapping system, which revealed a cross-contamination factor of $0.5 \pm 0.4\%$ (Agrios et al. 2015). Cross- and constant contamination tend to increase with the amount of packed granular material interacting with the CO_2. In our case, the Cu reduction reactor contains a lot of wire bits, which may explain the slightly higher cross-contamination. Nevertheless, the constant contamination is not affected in the same negative way.

Ambient Aerosol Filter Analysis

Figure 4 presents a proof-of-principle for the separation run of OC and EC for a selected winter sample from the urban background station Zurich. In a pure O_2 method, the OC fraction evolved in the first peak at 375°C and the more refractory, pure EC in the last temperature step (650°C). In between, the intermediate fraction at 475°C characterizes the transition from refractory OC with a more nonfossil signal to nonrefractory EC with a rather fossil signal as indicated by the decreasing trend of the ^{14}C/^{12}C ratio. The slope of the linear fitting has been used as a metric to evaluate to what extent the molecular components of distinct thermal fractions exhibit or not significantly different ^{14}C/^{12}C ratios and if the ^{14}C/^{12}C concentration is uniform within the fraction or subfraction. This metric is important for weighting if the thermal fraction needs further purification and better separation tuning. The ^{14}C/^{12}C slopes of the EC and OC fractions are small (<0.011) compared to the second step at 475°C. This second step reflects the transition from the initial step, which is enriched in OC and depleted in EC, to nearly pure EC at the final step. Consequently, we define, as a first approximation, that there is no significant ^{14}C shift if the slope is lower than 0.011. This threshold is protocol-dependent and more studies are required to arrive into a reliable value. The continuous-flow separation of Figure 4 highlights the importance of the intermediate temperature step to purify the EC on the one hand and the potential of the real-time online
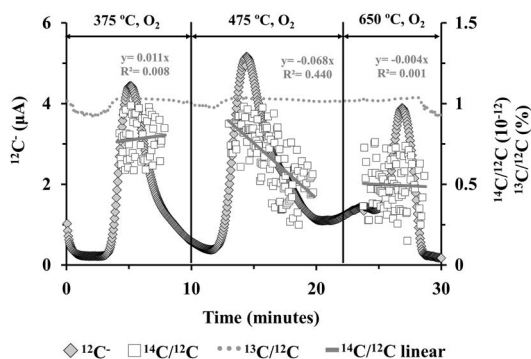
Figure 4 Continuous-flow $^{14}C/^{12}C$ measurement overlaid with the $^{12}C^{-}$ current and the $^{13}C/^{12}C$ ratio for an aerosol filter from Zurich from January 2008 treated with the OC/EC protocol consisting of three temperature ramps (375, 475, and 650°C) under pure oxygen. The elevated baseline after the second peak is due to an artifact of the measurement and has not been reproduced in other runs.

^{14}C analysis to uncover different fossil versus nonfossil signals of chemically similar aerosol fractions on the other hand.

Figure 5 shows two characteristic examples of real-time ^{14}C measurements of OC subfractions with modified temperature ramps. Taking in account the threshold slope of 0.011, Figure 5a shows that with the exception of the subfraction at 200°C, the $^{14}C/^{12}C$ ratio does not vary significantly throughout the thermal treatment for this winter sample from Zurich with substantial wood-burning emissions (Zotter et al. 2014b). The more fossil signal at the onset of the temperature ramp indicates that the wood-burning OC, which carries a purely nonfossil signal, is slightly more refractive than the fossil OC from the urban traffic. The situation is different for a spring sample from the Los Angeles Basin (Zotter et al. 2014a) shown in Figure 5b. Here, the OC peak is split thermally only into two subfractions, as the application of more thermal steps is not feasible when the filter loading is low. The volatile subfraction evolving in the first peak at 200°C is characterized by more fossil levels with a trend towards more nonfossil values for an increasing refractivity of the OC chemical species, which even continues into the second peak at 375°C. This is corroborated by the observation for the Los Angeles Basin that fresh SOA, which is more volatile, mainly originates from fossil emissions from the urban center, whereas aged (i.e. less volatile) SOA rather originates from a nonfossil rural background outside of the city (Zotter et al. 2014a). Table 2 compiles the examples from Figure 5 and further real-time ^{14}C analyses of OC subfractions with similar thermal behavior. Each row contains the values for one filter measured once. The isotopic data are the averages of the values laying inside the FWHM of the $^{12}C^{-}$ peak due to the good stability of the $^{13}C/^{12}C$ ratio in this range. From the linear fitting evaluation, only the measured thermal subfractions denoted by asterisks in the table demonstrate a significant difference in the $^{14}C/^{12}C$ concentration within the respective subfraction. Table 2 shows that the shift from fossil to nonfossil emissions in the first peak for the winter sample from Zurich was neither visible for Zurich during summer, nor for the rural station Sissach during winter. This may result from the absence of wood burning during summer for the former and smaller traffic contribution for the latter case (Zotter et al. 2014b). For the Los Angeles Basin, the additional cases from Table 2 behave differently than the sample from 20/05/2010, which is displayed in Figure 5b, probably because this sample is more influenced by the local urban plume than the other cases (Zotter et al. 2014a).
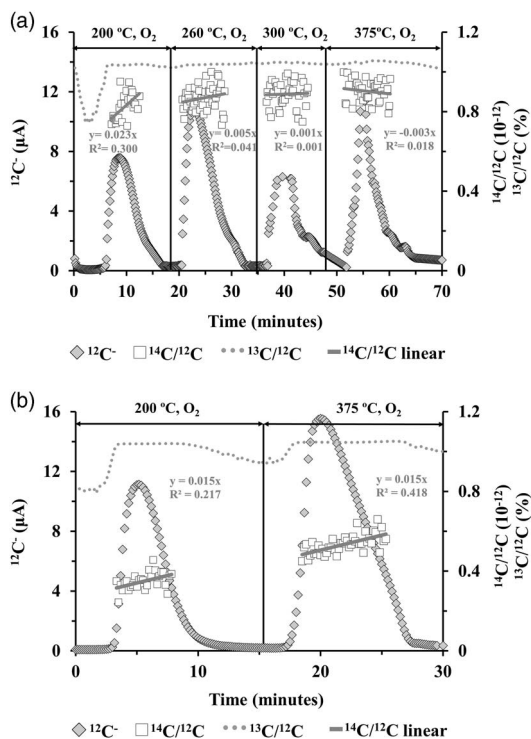
Figure 5 Continuous-flow $^{14}C/^{12}C$ analysis of OC subfractions (a) evolving at 200, 260, 300, and 375°C for an aerosol filter from Zurich for 28/01/2009; and (b) of OC subfractions evolving at 200 and 375°C for an aerosol filter from the Los Angeles Basin for 20/05/2010. Please note that both examples are also included in Table 2.

Table 2 ^{14}C real-time analysis of a selection of ambient aerosol filters from several campaigns. The $F^{14}C$ values are averaged over distinct CO_2 subfractions evolving at 200, 260, 300, and 375°C or 200 and 375°C. Each filter was measured only once. The uncertainty is related to the counting statistics. Statistically significant ^{14}C shifts within such subfractions are indicated with an asterisk. For the filters from the Los Angeles Basin, three 1.5-cm^2 quartz filter punches were piled up in the sample holder during combustion. ND means not detected.

		$F^{14}C$			
Location of sample	Date of collection	200°C	260°C	300°C	375°C
Zurich (Switzerland)	30/01/2008	0.637 ± 0.019*	0.843 ± 0.020	ND	0.936 ± 0.016
Zurich (Switzerland)	28/01/2009	0.772 ± 0.017*	0.843 ± 0.015	0.875 ± 0.019	0.876 ± 0.015
Zurich (Switzerland)	30/07/2009	0.677 ± 0.028			0.760 ± 0.024
Sissach (Switzerland)	30/02/2011	0.816 ± 0.020	0.840 ± 0.015	0.808 ± 0.017	0.858 ± 0.020
Los Angeles Basin (USA)	20/05/2010	0.329 ± 0.008*			0.494 ± 0.017*
Los Angeles Basin (USA)	24/05/2010	0.735 ± 0.014			0.803 ± 0.021
Los Angeles Basin (USA)	4/6/2010	1.038 ± 0.017			1.016 ± 0.019
Los Angeles Basin (USA)	6/6/2010	0.511 ± 0.011	0.592 ± 0.010	0.593 ± 0.022	0.599 ± 0.021

CONCLUSIONS AND OUTLOOK

A continuous-flow interface for ^{14}C AMS is described that allows a commercial Sunset OC/EC analyzer to be coupled to a MICADAS gas ion source. Dimensions of the transfer capillary and target boreholes as well as the He carrier gas flow are optimized such that carbon masses are adjusted in order to prevent ^{12}C$^-$ signal suppression, and the response of the system in the analysis of very small samples is satisfactory. This allows for the first time to measure efficiently ambient atmospheric aerosol combustion products by ^{14}C AMS in real-time mode, revealing the potential of real-time online ^{14}C analysis of chemically similar subfractions that are not possible to be disentangled by conventional thermo-optical methods. Future studies will focus on the evaluation of the peak-to-peak memory by combusting known mixtures of fossil and modern materials in a modified temperature ramp as well as on the usage of targets with intermediate ID borehole sizes as to optimize further the CO_2 proportion to carrier gas.

REFERENCES

Agrios K, Salazar G, Zhang YL, Uglietti C, Battaglia M, Luginbühl M. 2015. Online coupling of pure O$_2$ thermo-optical methods – ^{14}C AMS for source apportionment of carbonaceous aerosols. *Nuclear Instruments and Methods in Physics Research B* 361:288–93.

Currie LA, Kessler JD. 2005. On the isolation of elemental carbon (EC) for micro-molar ^{14}C accelerator mass spectrometry: development of a hybrid reference material for ^{14}C–EC accuracy assurance, and a critical evaluation of the thermal optical kinetic (TOK) EC isolation procedure. *Atmospheric Chemistry and Physics* 5:2833–45.

De Gouw J, Jimenez L. 2009. Organic aerosols in the Earth's atmosphere. *Environmental Scientific Technology* 43:7614–8.

Fahrni SM, Wacker L, Synal H-A, Szidat S. 2013. Improving a gas ion source for ^{14}C AMS. *Nuclear Instruments and Methods in Physics Research B* 294:320–7.

Hodzic A, Jimenez JL, Prévôt ASH, Szidat S, Fast JD, Madronich S. 2010. Can 3-D models explain the observed fractions of fossil and non-fossil carbon in and near Mexico City? *Atmospheric Chemistry and Physics* 10(22):10,997–16.

Kanakidou M, Seinfeld JH, Pandis SN, Barnes I, Dentener FJ, Facchini MC, Van Dingenen R, Ervens B, Nenes A, Nielsen CJ, Swietlick E, Putaud JP, Balkanski Y, Fuzzi S, Horth J, Moortgat GK, Winterhalter R, Myhre CEL, Tsigaridis K, Vignati E, Stephanou EG, Wilson J. 2005. Organic aerosol and global climate modelling: a review. *Atmospheric Chemistry and Physics* 5:1053–123.

Le Clercq M, van der Plicht J, Gröning M. 1998. New ^{14}C reference materials with activities of 15 and 50 pMC. *Radiocarbon* 40(1):295–7.

Perron N, Szidat S, Fahrni S, Ruff M, Wacker L, Prévôt ASH, Baltensperger U. 2010. Towards on-line ^{14}C analysis of carbonaceous aerosol fractions. *Radiocarbon* 52(2–3):761–8.

Pöschl U. 2005. Atmospheric aerosols: composition, transformation, climate and health effects. *Angewandte Chemie International Edition* 44(46):7520–40.

Reimer P, Brown TA, Reimer R. 2004. Discussion: reporting and calibration of post-bomb ^{14}C data. *Radiocarbon* 46(3):1299–304.

Robinson AL, Donahue NM, Shrivastava MK, Weitkamp EA, Sage AM, Grieshop AP, Lane TE, Pierce R, Pandis SN. 2007. Rethinking organic aerosols: semi-volatile emissions and photochemical aging. *Science* 315(5816):1259–62.

Rozanski K, Stichler W, Gonfiantini R, Scott EM, Beukens RP, Kromer B, van der Plicht J. 1992. The IAEA ^{14}C Intercomparison Exercise 1990. *Radiocarbon* 34(3):506–19.

Ruff M, Fahrni SM, Gäggeler HW, Hajdas I, Suter M, Synal H-A, Szidat S, Wacker L. 2010. Online radiocarbon measurements of small samples using elemental analyzer and MICADAS gas ion source. *Radiocarbon* 52(4):1645–56.

Salazar G, Zhang YL, Agrios K, Szidat S. 2015. Development of a method for fast and automatic radiocarbon measurement of aerosol samples by online coupling of an elemental analyzer with a MICADAS AMS. *Nuclear Instruments and Methods in Physics Research B* 361:163–7.

Salazar G, Agrios K, Eichler R, Szidat S. 2016. Characterization of the axial jet separator with a CO_2/helium mixture: toward GC-AMS hyphenation. *Analytical Chemistry* 88:1647–53.

Szidat S. 2009. Sources of Asian haze. *Science* 323(5913):470–1.

Szidat S, Jenk TM, Gäggeler HW, Synal H-A, Fisseha R, Baltensperger U, Kalberer M, Samburova V, Reimann S, Kasper-Giebl A, Hajdas I. 2004a. Radiocarbon (^{14}C)-deduced biogenic and anthropogenic contributions to organic carbon (OC) of urban aerosols from Zürich, Switzerland. *Atmospheric Environment* 38(24):4035–44.

Szidat S, Jenk TM, Gäggeler HW, Synal H-A, Hajdas I, Bonani G, Saurer M. 2004b. THEODORE, a two-step heating system for the EC/OC determination of

radiocarbon (^{14}C) in the environment. *Nuclear Instruments and Methods in Physics Research B* 223–224:829–36.

Szidat S, Jenk TM, Synal H-A, Kalberer M, Wacker L, Hajdas I, Kasper-Giebl A, Baltensperger U. 2006. Contributions of fossil fuel, biomass-burning, and biogenic emissions to carbonaceous aerosols in Zurich as traced by ^{14}C. *Journal of Geophysical Research* 111(D7):D07206.

Szidat S, Salazar G, Vogel E, Battaglia M, Wacker L, Synal H-A, Türler A. 2014. ^{14}C analysis and sample preparation at the new Bern Laboratory for the Analysis of Radiocarbon with AMS (LARA). *Radiocarbon* 56(2):561–6.

Wacker L, Fahrni SM, Hajdas I, Molnar M, Synal H-A, Szidat S, Zhang YL. 2013. A versatile gas interface for routine radiocarbon analysis with a gas ion source. *Nuclear Instruments and Methods in Physics Research B* 294:315–9.

Zhang YL, Perron N, Ciobanu VG, Zotter P, Minguillon MC, Wacker L, Prevot ASH, Baltensperger U, Szidat S. 2012. On the isolation of OC and EC and the optimal strategy of radiocarbon-based source apportionment of carbonaceous aerosols. *Atmospheric Chemistry and Physics* 12(22): 10841–56.

Zotter P, Ciobanu VG, Zhang YL, El-Haddad I, Macchia M, Daellenbach KR, Salazar GA, Huang RJ, Wacker L, Hueglin C, Piazzalunga A, Fermo P, Schwikowski M, Baltensperger U, Szidat S, Prévôt ASH. 2014a. Diurnal cycle of fossil and nonfossil carbon using radiocarbon analyses during CalNex. *Journal of Geophysical Research: Atmospheres* 119:6818–35.

Zotter P, Ciobanu VG, Zhang YL, El-Haddad I, Macchia M, Daellenbach KR, Salazar G, Huang RJ, Wacker L, Hueglin C, Piazzalunga A, Fermo P, Schwikowski M, Baltensperger U, Szidat S, Prévôt ASH. 2014b. Radiocarbon analysis of elemental and organic carbon in Switzerland during winter-smog episodes from 2008 to 2012 – Part 1: source apportionment and spatial variability. *Atmospheric Chemistry and Physics* 14(13):551–70.